



A method for estimating lithium-ion battery state of health based on physics-informed machine learning

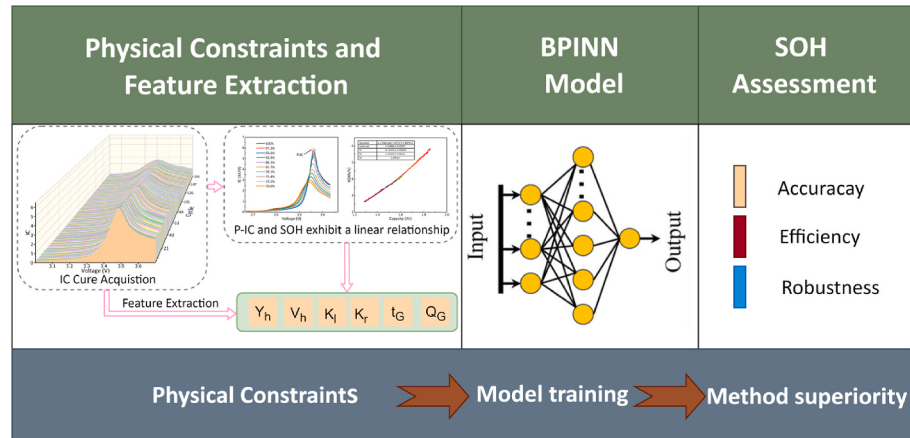
Guoqing Sun, Yafei Liu, Xuewen Liu*

School of Mechanical and Automotive Engineering, Shanghai University of Engineering Science, Shanghai 201600, China

HIGHLIGHTS

- Key features are derived from the incremental capacity (IC) curve.
- Peak IC and battery health are incorporated as a physical constraint.
- Secondary optimization enhances the accuracy of FNN predictions using physical principles.
- The method is validated with datasets from NASA and Oxford University.

GRAPHICAL ABSTRACT



ARTICLE INFO

Keywords:

Lithium-ion battery
State of health
Physics-informed neural network
Physical constraint
Incremental capacity curve

ABSTRACT

Data-driven approaches are widely applied in estimating the State of Health (SOH) of Lithium-Ion Batteries (LIB). However, these methods often suffer from a lack of interpretability. To address this issue, this article proposes a method called Battery Physics-Informed Neural Network (BPINN) to enhance the interpretability of the Feed-forward Neural Network (FNN) in SOH prediction. This article is based on the concept of Physics-Informed Neural Networks (PINN). Features are initially extracted from Incremental Capacity (IC) curves to characterize the battery aging process. Notably, IC curve peaks (P-IC) reflect electrochemical reactions during charge and discharge cycles. The degradation of these peaks is directly related to the loss of active materials, causing SOH reduction. This article transforms the monotonic relationship between P-IC and SOH into a physical constraint, which is embedded into model training. Furthermore, during prediction, a secondary "training" based on physical constraints is applied to the FNN prediction results, enhancing the model's interpretability and accuracy. The proposed method is validated using publicly available battery datasets from NASA and the University of Oxford. Results show BPINN effectively improves SOH prediction accuracy, reducing the Mean Absolute Error (MAE) and Root Mean Square Error (RMSE) to below 0.4 %.

* Corresponding author.

E-mail address: xuewen2018@126.com (X. Liu).

1. Introduction

Lithium-ion batteries (LIB) have become increasingly prevalent as one of the crucial energy storage systems in modern society and are regarded as a key technology for achieving sustainable development goals [1,2]. LIBs possess advantages such as high energy density, high specific energy, low pollution, and low energy consumption [3], making them the preferred choice for numerous electronic devices and clean energy solutions. However, the complex internal electrochemical characteristics of LIB, coupled with the diversity and complexity of their application environments, render their degradation process challenging to predict [4–6]. Battery failure not only increases maintenance costs but can also lead to severe consequences, resulting in economic losses [7]. Therefore, predicting and managing the SOH of LIB is of paramount importance [8]. The Battery Management System (BMS), as a core component of battery technology [9], is responsible for ensuring safe, reliable, and efficient battery operation, extending its service life, and collecting data to support the optimization and maintenance of battery systems. State monitoring is a fundamental function of BMS [10], which includes estimating the State of Charge (SOC), SOH, State of Energy (SOE), and State of Power (SOP). SOH reflects the degree of performance degradation during the battery's charge-discharge cycles [11] and is one of the critical parameters affecting battery reliability and safety, particularly crucial for electric vehicles equipped with LIB. Consequently, accurate estimation of the SOH of LIB is vital for BMS.

1.1. Literature review

Methods for estimating the SOH of LIB can be mainly divided into two categories: Physics-Based Models (PBM) and data-driven approaches. PBMs typically rely on physical or mathematical models to simulate battery operating mechanisms and evaluate their performance and lifespan. For instance, Liang et al. [12] proposed a hybrid method combining deep neural networks and a double exponential model to predict battery remaining useful life (RUL). In experiments using NASA's public dataset, this method achieved a RUL prediction error below 1.5 %, demonstrating strong performance in long-life battery prediction. However, the method demands significant computational resources, has high model complexity, and requires lengthy training times. Prada et al. [13] introduced a simplified electrochemical-thermal model that combines an extended Kalman filter, exhibiting excellent performance in fast-charging applications. Experimental data indicate that the method achieves SOH estimation errors below 1 % across various charging rates. By accounting for thermal effects, it notably enhances the accuracy of battery performance assessment. Chen et al. [14] developed an electrochemical-thermal-aging coupled model capable of simulating lithium-ion battery performance and estimating SOH. In experiments involving various battery types, the method achieved SOH prediction errors under 0.5 %. It effectively captures how physical processes during battery aging affect performance. Kim et al. [15] utilized a multi-scale, multi-physics model to accurately predict capacity degradation and internal impedance growth in lithium batteries. Experimental data demonstrate an SOH estimation error of approximately 1.2 %. The model effectively reflects internal physical changes within the battery in both experimental and numerical simulations. Additionally, equivalent circuit models combined with recursive least squares and unscented Kalman filters can be used to estimate battery states and correlate SOH with irreversible lithium loss [16]. However, PBM methods face challenges in practical applications. Firstly, the accuracy of PBMs largely depends on the applicability of the chosen model, and most physical models have limitations in fully capturing the complex degradation mechanisms and electrochemical behaviors of LIB, especially in some special or extreme conditions. Secondly, PBM methods typically require high-quality measurement data and are sensitive to noise in the measurement process, which is difficult to guarantee in practical applications. Therefore, although PBMs can provide

relatively accurate SOH estimates, their model complexity and computational resource requirements limit their feasibility in practical applications.

In recent years, data-driven methods have made significant progress in the field of lithium-ion battery SOH estimation [17,18]. These methods do not require an in-depth understanding of battery aging mechanisms [19] but instead infer battery health status by analyzing historical data such as current, voltage, capacity, and impedance parameters [20]. Due to their ease of implementation, data-driven methods have gained increasing attention. For instance, Peng et al. [21] introduced an LSTM network-based SOH estimation method that extracts multiple health features. In experiments using the NASA battery dataset, the method achieved an SOH estimation error below 1 %. LSTM networks excel at processing time-series data, enabling them to capture subtle changes during battery operation. Pan et al. [22] presented a method combining two-stage feature extraction with gradient boosting decision trees. By comprehensively analyzing multiple features, they achieved an average SOH prediction error of 3 % on the Oxford battery dataset. Experiments also indicate that the method significantly improves model robustness when processing aging data. Furthermore, Ma et al. [23] introduced a personalized SOH estimation method based on transfer learning with strong generalization across different battery types. In experiments, by transferring pre-trained models, the method reduced SOH prediction errors by 10 %–15 %. It effectively resolves the issue of variability among battery types. Yao et al. [24] proposed a graph neural network-based framework that effectively models complex internal state relationships in batteries. Experimental results indicate an SOH prediction error below 0.2 % on public datasets. Under noisy data conditions, the prediction error increased by only 0.2 %. Dai et al. [25] introduced a neural network method based on Markov chains and prior knowledge that can dynamically update the SOH prediction model. In multiple cyclic charge-discharge experiments, the prediction error remained stable between 0.5 % and 1.7 %, indicating high flexibility and accuracy. In addition to these advancements, new computational methodologies based on AI have also shown promise in the fields of materials science and energy storage. For example, recent studies have demonstrated AI-driven approaches for predicting the remaining useful life of supercapacitors under various conditions and fault detection in battery systems [26–29]. However, data-driven methods also have inherent limitations. As they do not rely on a deep understanding of battery aging mechanisms and often involve dimensionality reduction and feature engineering [30], their prediction results may contradict physical principles, leading to a lack of interpretability and physical plausibility. Moreover, purely data-driven models often lack predictive interpretability, making it difficult to reveal the underlying physical mechanisms behind their predictions.

Physics-informed machine learning (PIML) offers an effective solution to the problem of insufficient interpretability in purely data-driven models. By integrating physical principles with data-driven methods, PIML utilizes prior physical knowledge to guide and enhance the performance of machine learning models. However, existing PIML approaches face challenges when handling complex nonlinear systems, such as SOH prediction of lithium-ion batteries. For example, due to noise, nonlinear complexities, and dynamic operating conditions in real-world data, current PINN models may struggle to effectively capture all physical processes. This can lead to predictions lacking physical consistency or adaptability. In recent years, explanation methods in machine learning, particularly deep learning, have gained attention for improving model interpretability. These methods are generally divided into ante-hoc and post-hoc techniques. Ante-hoc methods, like model-driven deep unrolling, aim to design interpretable models by structuring neural networks to mirror iterative optimization algorithms or physical processes. Post-hoc methods, such as feature importance visualization or saliency maps, interpret trained models by highlighting key input features influencing predictions. While these methods improve interpretability, they often require additional tools for analysis. In

contrast, the proposed BPINN enhances interpretability inherently by embedding physical constraints into the training process, ensuring that the model's predictions are physically consistent and transparent. Kohtz et al. [31] proposed a deep neural network model incorporating physical constraints by integrating battery physical laws into model training. While this method improved prediction accuracy, it has limited adaptability under complex dynamic conditions. Hofmann et al. [32] applied physical information to impose prior knowledge constraints on Bayesian neural networks. Although this enhanced the model's uncertainty estimation capability, significant prediction errors occurred when data contained high noise or under non-standard operating conditions. Wang et al. [33] applied PINN for stable SOH estimation across diverse battery types, achieving strong generalization but still facing challenges with noise and dynamic operating conditions. Vilsen et al. [34] introduced a physics-driven transfer learning method that improved model generalization. However, performance degradation still existed when transferring between different battery types. Ye et al. [35] studied a physics-constrained reinforcement learning method that effectively optimized SOH prediction strategies under complex working conditions. Yet, the model may exhibit weaker robustness under highly complex or non-standard battery operating conditions. To overcome these issues, this paper proposes the BPINN method. The model enhances physical consistency by embedding the monotonic relationship between P-IC and SOH during battery aging as physical constraints into model training. Additionally, the model's performance is further optimized through secondary training to address the decline in prediction accuracy under complex operating conditions. Compared with existing methods, BPINN not only improves model interpretability but also enhances predictive ability and adaptability under complex battery aging conditions. The effectiveness of the model is validated using datasets from NASA and the University of Oxford. Results show that BPINN outperforms existing PINN models in both prediction accuracy and physical consistency.

1.2. Contributions

Changes in P-IC reflect the dynamic processes of electrochemical reactions within the battery, particularly the charge transfer at the electrode-electrolyte interface and the formation and growth of impedance and solid electrolyte interphase (SEI) films during battery cycling [36]. As the number of cycles increases, the gradual consumption of active materials and structural degradation within LIBs lead to significant changes in P-IC, directly affecting the battery's charge-discharge efficiency and capacity retention rate. Consequently, a strong monotonic relationship exists between P-IC and SOH, allowing for the inference of battery health status through P-IC monitoring [37]. Specifically, as lithium-ion batteries undergo cyclic aging, IC peak values typically show a declining trend. This is attributed to the gradual deactivation of active materials and increased charge transfer impedance due to SEI film thickening [38,39]. Therefore, the reduction in P-IC can serve as a crucial indicator of SOH decline. This study aims to incorporate physical knowledge into data-driven models, a method for estimating the SOH of LIB based on a physically constrained neural network is proposed. This approach transforms the monotonic relationship between P-IC and SOH into physical constraints to guide model training. It further optimizes the model through a secondary "training" process, enhancing the model's interpretability and prediction accuracy. The specific contributions are as follows:

- (1) The monotonic relationship between P-IC and SOH is incorporated as a physical constraint.
- (2) A physics-constrained secondary "training" effectively enhances the interpretability and prediction accuracy of the FNN.
- (3) To evaluate the performance of the BPINN model, experiments were conducted on both NASA and University of Oxford battery datasets. Analysis was performed on the guiding role of physical constraints in model training, as well as the improvements in

model prediction accuracy and interpretability resulting from the secondary "training" process.

1.3. Organization of the paper

The remainder of this paper is organized as follows. Section 2 introduces the research methodology. Section 3 provides a detailed overview of the experiments and analysis. Conclusions are summarized in Section 4.

2. Research methodology

As illustrated in Fig. 1, this study proposes a BPINN-based method for estimating the SOH of LIB, aimed at improving prediction accuracy and interpretability. The core concept of this method is to integrate the physical laws governing battery aging processes into both the training and prediction phases of the neural network. This approach constrains the model's learning process, ensuring that its predictions align more closely with physical reality. The method is primarily divided into three stages: data preprocessing and feature engineering, physics-constrained model training, and physics-constrained secondary "training". Initially, the IC curves are extracted from battery discharge data, from which key features are then derived. These features effectively characterize the battery aging process. Subsequently, a feedforward neural network is constructed with the extracted features as inputs and SOH as the output. The monotonic relationship between P-IC and SOH is transformed into a physical constraint and embedded into the loss function, guiding the model training process. Finally, during the testing phase, the trained neural network model undergoes a physics-constrained secondary optimization. This secondary "training" further adjusts the model parameters, aligning its predictions more closely with the battery's physical characteristics. This step not only enhances prediction accuracy but also improves the model's interpretability.

2.1. Feature extraction from IC curves

This study employs the publicly available battery dataset provided by NASA [40] to validate the proposed SOH estimation method. The dataset includes full lifecycle data for four different models of 18650 lithium-ion batteries (labeled B0005, B0006, B0007, and B0018) under various operating conditions. The positive electrode material for batteries B0005, B0006, and B0007 is lithium nickel cobalt aluminum oxide (NCA), and the negative electrode material is graphite, with a nominal capacity of 2 A h. Battery B0018 uses lithium nickel manganese cobalt oxide (NMC) as the positive electrode material and graphite as the negative electrode material, with a nominal capacity of 1.35 A h. All batteries were charged using the constant current constant voltage (CC-CV) method. The charging current was set at 1.5 A, with a cutoff voltage of 4.2 V and a cutoff current of 20 mA. For discharging, batteries B0005, B0006, and B0007 had a discharge current of 2 A, with cutoff voltages of 2.7 V, 2.5 V, and 2.2 V, respectively. Battery B0018 had a discharge current of 1.5 A and a cutoff voltage of 2.5 V. The voltage and current profiles for the entire test cycle of battery B0005 are shown in Fig. 2(a). All charging and discharging cycles were conducted at room temperature (24 °C). The data acquisition system recorded parameters such as voltage, current, and temperature at a sampling frequency of 1 Hz. In this study, SOH is defined as the ratio of the current maximum available capacity to the rated capacity, as shown in equation (1).

$$SOH = \frac{Q_{actual}}{Q_{nominal}} \times 100\% \quad (1)$$

where Q_{actual} is the current maximum available capacity and $Q_{nominal}$ is the rated capacity.

Fig. 2(b) illustrates the capacity degradation curves of four different battery models in the NASA dataset as a function of the number of

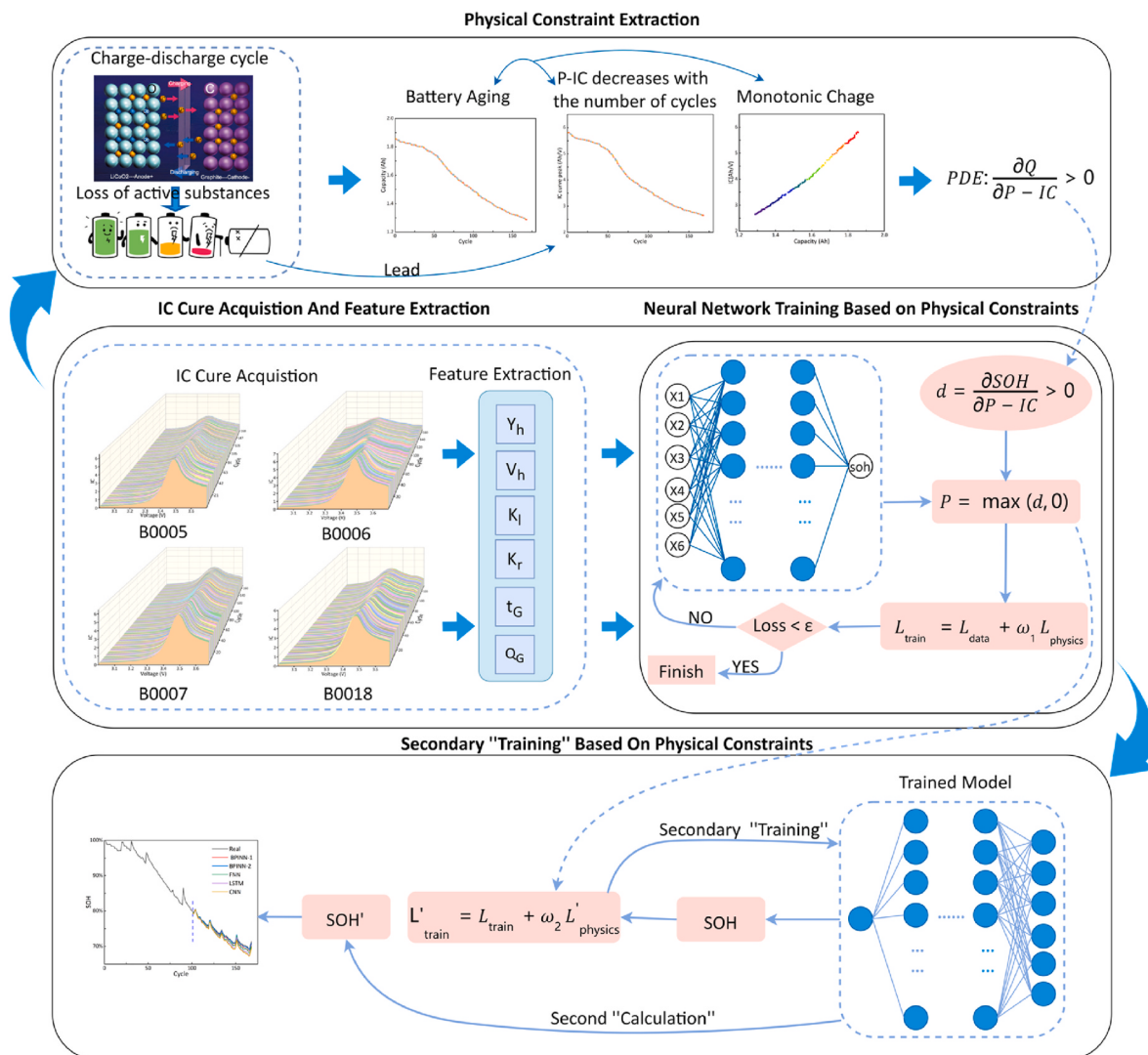


Fig. 1. Flowchart of the BPINN for battery SOH estimation.

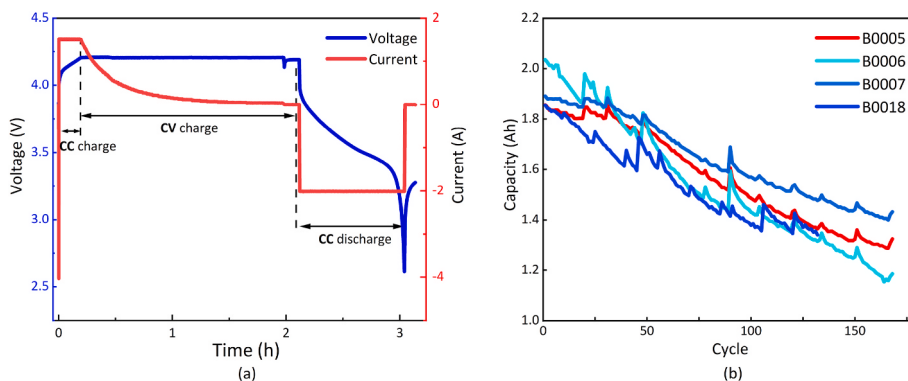


Fig. 2. Battery Cycling and Capacity Degradation Curves: (a) Voltage and current profiles over the entire test cycle for Battery B0005. (b) Capacity degradation trends for the four different battery models as a function of the number of cycles.

cycles. It can be observed that the capacity of each battery gradually decreases with the increase in the number of cycles.

The IC curve of LIB contains extensive information about battery aging and can be used to reveal aging mechanisms. For instance, Zheng et al. [41] discovered that, as the number of cycles increases, the main peak of the IC curve for LiCoO₂ batteries gradually shifts towards higher

voltages, and the peak height decreases. The area under the peak is directly related to the battery's capacity; aging of the battery leads to the loss of active material and capacity degradation, which in turn reduces the peak area [42]. The thickening of the SEI film can impede lithium ions from embedding into the anode material, causing a faster voltage increase at the initial stage of charging, thus flattening the slope on the

left side of the IC curve [43]. The loss of active material results in a decrease in battery capacity, which causes a faster voltage drop towards the end of discharge, making the slope on the right side of the IC curve steeper [44], and thereby shortening the discharge time [45].

IC Curve Acquisition: The IC curve is a widely recognized tool for analyzing battery capacity degradation. It can be obtained by differentiating the voltage and capacity data collected during the constant current charging process. Specifically, the IC curve describes the incremental changes in battery capacity over consecutive voltage steps. Given the constant charging current, the battery capacity and voltage can be calculated using the following formula:

$$Q = It \quad (2)$$

$$V = f(Q), Q = f^{-1}(V) \quad (3)$$

where I is the charge current, t is the charge time, and V is the battery voltage. According to Equation (2), the IC curve can be expressed as follows:

$$(f^{-1})' = \frac{dQ}{dV} = \frac{Idt}{dV} = I \frac{dt}{dV} \quad (4)$$

To minimize the impact of noise on the calculation of the IC curve, a finite difference method is employed to approximate the IC curve from a mathematical perspective.

$$\frac{dQ}{dV} \Big|_k \approx \frac{\Delta Q_k}{\Delta V_k} = \frac{Q_k - Q_{k-1}}{V_k - V_{k-1}} \quad (5)$$

where Q_k and Q_{k-1} represent the battery's charge capacity at time steps k and $k-1$, respectively, and V_k and V_{k-1} represent the battery's terminal voltage at time steps k and $k-1$, respectively. To further reduce the impact of noise, the calculated IC curve was smoothed using a Gaussian filter.

IC curve analysis serves as a powerful diagnostic tool for revealing internal electrochemical changes during lithium-ion battery aging, providing valuable insights into the underlying mechanisms of battery degradation. The IC curve reflects the relationship between the rate of capacity change and voltage, with its characteristic changes closely linked to battery performance deterioration. The aging of lithium-ion batteries manifests as a gradual decline in performance, rooted in various complex physicochemical processes such as current collector corrosion, lithium dendrite growth, and electrolyte decomposition. These aging processes leave unique "fingerprints" on the IC curve, including reduced peak heights, shifted peak positions, increased peak widths, and increased internal resistance [46]. By analyzing these characteristic changes, the degree and type of battery aging can be effectively identified. The advantage of IC curve analysis lies in its ability to delve into the battery electrode level, revealing reaction mechanisms during lithium-ion insertion and extraction processes. Notably, the IC curve can convert battery voltage plateaus into distinct P-IC peaks, each corresponding to specific electrochemical reactions, such as phase transitions or insertion and extraction processes of different types of active materials. Consequently, IC curve analysis is considered one of the key techniques for studying lithium-ion battery aging mechanisms, providing crucial evidence for battery performance evaluation and lifespan prediction.

To illustrate the trends in IC curves during battery aging more clearly, this paper analyzes the IC curves during charge-discharge cycles using the B0005 dataset from the NASA battery dataset as an example. These curves are used to characterize capacity decay and changes in electrochemical properties during the battery aging process. As shown in Fig. 3(a), these characteristics include: P-IC (y_h), peak position (V_h), left peak slope (k_l), right peak slope (k_r), peak area (Q_G), and discharge time (t_G). A fixed voltage width of $\Delta_v = 0.1$ V is used [47]. The highest point of the IC curve is y_h , with the corresponding x-coordinate V_h . The three features k_l , k_r , and t_G are obtained using the following formulas (6-8):

$$V_l = V_h - \frac{\Delta_v}{2}, V_r = V_h + \frac{\Delta_v}{2} \quad (6)$$

$$k_l = \frac{y_h - y_l}{V_h - V_l}, k_r = \frac{y_h - y_r}{V_h - V_r} \quad (7)$$

$$t_G = t_r - t_l \quad (8)$$

where t_r is the discharge time of voltage V_r , and t_l is the discharge time of voltage V_l .

As shown in Fig. 3(a), as the degree of battery aging increases, the IC curve becomes smoother and exhibits a more gradual trend, with the P-IC gradually decreasing.

The decrease in P-IC is closely related to the loss of active materials within the lithium-ion battery. With the increase in charge-discharge cycles, the active materials gradually degrade, becoming less effective in accommodating lithium ions. This reduction in electrochemically active materials leads to battery performance degradation. The loss of active materials is one of the primary reasons for the decrease in battery capacity. Therefore, there is a monotonic relationship between P-IC and the battery's SOH, as illustrated in Fig. 3(b).

2.2. Physically constrained neural network

This study employs the FNN to evaluate and predict the SOH of LIB. As a deep learning model with a simple structure and ease of training, The FNN demonstrates significant advantages in handling complex nonlinear systems such as LIB. The FNN consists of three main components: an input layer, hidden layers, and an output layer. These layers transmit information sequentially, ultimately producing a prediction of the LIB's SOH. The network operates on the principle of forward propagation, where information flows from the input layer through a series of connections and computations to the output layer. The input layer receives raw data, such as the six features extracted in this study, with each feature corresponding to a neuron. During forward propagation, each neuron is connected to all neurons in the previous layer, with each connection associated with a weight and a bias. Weights represent the strength of connections, while biases determine the activation threshold of neurons. For each neuron, the network calculates a weighted sum, which is the cumulative result of the previous layer's outputs multiplied by their respective weights, plus the bias. This weighted sum is then input into an activation function, such as the sigmoid function, ReLU function, or tanh function, to convert it into a nonlinear output. This output, after being processed by the activation function, is used as the input for the next layer of neurons, and so on, until the final output layer. The result of the output layer is the predicted value of the LIB's SOH. The entire process can be understood as a flow of information, starting from the input data, passing through layer-by-layer connections and weight adjustments, and ultimately producing a predicted result. The formula for the weighted sum generated in this process is as follows:

$$z_i = \alpha \left(\sum_{j=1}^n W_{ij} x_j + b_i \right) \quad (9)$$

Where x_j represents the output of the j -th neuron in the input layer or the previous layer, W_{ij} denotes the weight from the j -th neuron in the previous layer to the i -th neuron in the current layer, and b_i represents the bias of the i -th neuron in the current layer. $\sum_{j=1}^n W_{ij} x_j$ signifies the total weighted sum, where n is the number of neurons in the previous layer. α denotes the activation function, which is a nonlinear function that converts the weighted sum into the output of the current neuron. z_i represents the output of the i -th neuron in the current layer. To endow the model with nonlinear learning capabilities, the neuron output undergoes processing by an activation function. The purpose of the activation function is to transform the linear weighted sum into a nonlinear output, enabling the neural network to model complex data patterns.

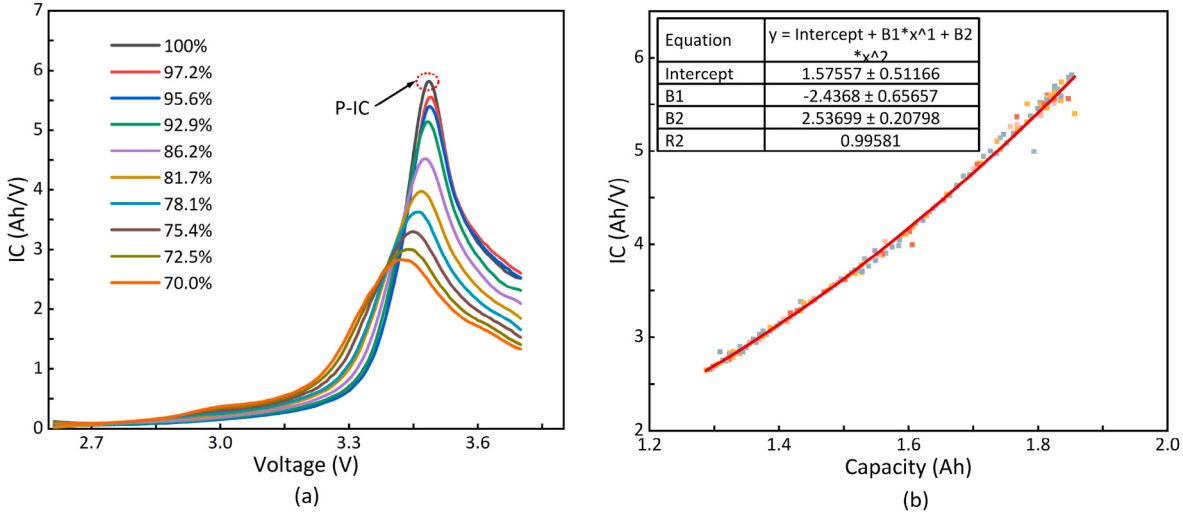


Fig. 3. Changes in IC Curve and Relationship Between Battery Capacity and P-IC: (a) The changes in the IC curve with battery aging. (b) The relationship between battery capacity and P-IC.

This process begins at the input layer, passing information through each layer until reaching the output layer. In each layer, every neuron performs a linear transformation on the input data based on its connection weights and bias, and then applies an activation function to generate a nonlinear output. This layer-by-layer computational process is referred to as forward propagation. When information flows through all the layers of the network, the forward propagation process completes, and the output layer generates the final prediction result. Next, the predicted result is compared with the actual label to calculate the loss function, which assesses the model's performance during training. The loss function measures the prediction error of the model and provides guidance for subsequent weight adjustments.

The core of the backpropagation algorithm is to adjust the network parameters using the gradient descent method to minimize prediction error. Firstly, the input data is passed through the network via forward propagation to obtain the prediction results. Then, the loss function is calculated to evaluate the difference between the predicted results and the actual labels. Next, the backpropagation algorithm starts from the output layer and progressively traces back to the input layer. The algorithm calculates the contribution of each weight and bias to the loss function using the chain rule, which means calculating the gradient of each parameter. Finally, using gradient descent or its variants, the network's weights and biases are updated based on the computed gradients. The update direction is opposite to the gradient direction, aiming to minimize the loss function. The entire training process iteratively performs forward propagation, loss function calculation, backpropagation, and parameter updates until the loss function converges or a preset stopping condition is reached.

To enhance the interpretability of the fully connected neural network, we introduced physical constraints to guide model training. These constraints are derived from an understanding of physical laws and can improve the model's accuracy and interpretability. As mentioned above, we know that there is a monotonic relationship between P-IC and the SOH of LIB. We can translate this physical information into constraint conditions and integrate it into the neural network's loss function. In this way, we guide the model to follow physical laws during the learning process, thereby improving the model's reliability and interpretability.

Traditional fully connected neural networks typically use mean squared error as the loss function to measure the difference between the model's predicted results and the actual values. The formula is as follows:

$$L_{\text{data}} = \frac{1}{2} \sum_{i=1}^N e_i^2 = \frac{1}{2} \sum_{i=1}^N (g(x^i, W, M) - H_i)^2 \quad (10)$$

Where N represents the number of samples in the training dataset, W denotes the parameter vector of the neural network model, M represents the structure of the neural network model, g denotes the output function, and H_i represents the actual SOH value of the i -th sample. We integrate the physical constraints into the loss function using the following formula:

$$d(x^i) = \frac{\partial \hat{g}(x^i, W, M)}{\partial x_1^i} > 0 \quad (11)$$

Where \hat{g} represents the neural network model's predicted value for x^i , x^i represents the P-IC feature value, and $d(x^i)$ represents the physical constraint learned based on the P-IC feature value.

The following loss function can be used to solve the constrained optimization problem in equation (10) to obtain the optimal solution:

$$L_{\text{physics}} = \sum_{i=1}^N [\min(0, d(x^i))]^2 \quad (12)$$

Ultimately, the physically constrained loss function can be expressed in the following form:

$$\min L_{\text{train}} = \min (L_{\text{data}} + \omega_1 L_{\text{physics}}) \quad (13)$$

To further enhance the interpretability of our model, we emphasize that integrating physical constraints not only improves accuracy but also provides a clear rationale for the model's predictions. By embedding well-established electrochemical principles, such as the monotonic relationship between the P-IC and SOH, into the training process, the BPINN ensures that its outputs are not just mathematically optimal but physically meaningful. This makes the model inherently interpretable, as each prediction aligns with known physical behaviors of lithium-ion batteries. Unlike traditional data-driven models, which often rely on post-hoc methods to explain predictions, our approach offers interpretability by design, meaning that the reasoning behind the model's decisions is transparent and directly related to the underlying physical laws. The secondary training phase further enhances this by refining predictions in alignment with these constraints, ensuring that the model's outputs adhere more closely to known degradation mechanisms.

2.3. Online optimization during the testing phase

Although the neural network can learn certain physical constraints during training, it may still produce predictions that do not conform to physical laws during the testing phase. To maintain consistent prediction accuracy during the testing phase, we introduced an online learning mechanism. This mechanism dynamically adjusts the model parameters based on the test data to ensure better adherence to the predefined physical constraints. This online learning mechanism effectively enhances the model's generalization ability and improves its interpretability and prediction accuracy in practical application scenarios. The specific method is as follows:

- (1) To evaluate the model's generalization ability, we use the test dataset to make predictions with the trained neural network and calculate the physical loss based on these predictions. This loss measures the deviation between the model's predictions and the physical constraints.

$$\left\{ \begin{array}{l} L'_{\text{physics}} = \sum_{i=1}^N [\min(0, \hat{d}(x^i))]^2 \\ \hat{d}(x^i) = \frac{\partial \hat{g}(x^i, W, M)}{\partial x^i} > 0 \end{array} \right. \quad (14)$$

Where $\hat{d}(x^i)$ represents the physical constraint learned based on the P-IC feature value in the test set, and L'_{physics} denotes the physical constraint loss.

- (2) To ensure that the model adheres more closely to physical constraints during the testing phase, we perform a second "training" and define a loss function that consists of two parts. The first part penalizes the error between the model's predicted values and the actual values from the training set, as well as penalizes violations of the physical constraints. The second part specifically penalizes violations of physical constraints in the predictions during the testing phase. By minimizing these two parts of the loss, the prediction accuracy and reliability of the model during the testing phase can be effectively improved. The loss function for the second 'training' is formulated as follows:

$$\left\{ \begin{array}{l} L'_{\text{train}} = L_{\text{train}} + L_{\text{test}} \\ L_{\text{train}} = L_{\text{data}} + \omega_1 L_{\text{physics}} \\ L_{\text{test}} = \omega_2 L'_{\text{physics}} \end{array} \right. \quad (15)$$

Where L_{physics} represents the physical loss of the BPINN on the training set predictions, measuring the degree to which the model violates physical constraints during training, and L'_{physics} represents the physical loss of the BPINN on the test set predictions. This method ensures that the model's predictions during the testing phase adhere more closely to physical laws while retaining the knowledge learned during training. Specifically, during the testing phase, we perform a second training of the model, combining the physical losses L_{physics} and L'_{physics} from both the training and test sets to fine-tune the model. This approach effectively improves the model's prediction accuracy and interpretability, ensuring it conforms more closely to physical laws and is more reliable in practical application scenarios.

3. Experiments and analysis

To evaluate the prediction performance and generalization of the BPINN, we compared it with several other neural network models, including Convolutional Neural Networks (CNN), LSTM, and FNN. The comparative experiments are based on battery datasets from NASA and

Oxford University, using two common evaluation metrics: Mean Absolute Error (MAE) and Root Mean Square Error (RMSE). MAE reflects the average error between the model's predicted values and the actual values, while RMSE reflects the standard deviation of the differences between the predicted values and the actual values. By comparing the MAE and RMSE values of different models, we can more comprehensively assess the prediction accuracy of the models. The formulas for calculating MAE and RMSE are as follows:

$$MAE = \frac{1}{N} \sum_{i=1}^N |\hat{y}_i - y_i| \quad (16)$$

$$RMSE = \sqrt{\frac{1}{N} \sum_{i=1}^N (\hat{y}_i - y_i)^2} \quad (17)$$

Where N is the number of samples to be evaluated, and y_i and \hat{y}_i are the actual values and estimated values, respectively.

3.1. Evaluation and validation with the NASA battery dataset

This study focuses on the experimental analysis of four LIB samples from the NASA battery dataset. The experimental design employed a data partitioning strategy, utilizing the first 60 % of each LIB dataset for model training and the remainder for performance testing. The model architecture consisted of three hidden layers, each containing 10 neurons. Physical constraints were incorporated into the training process to enhance the model's learning effectiveness. Specifically, the weight parameters ω_1 and ω_2 for the physical loss function were both set to 0.01. The Adam algorithm was used for optimization, with a fixed learning rate of 0.001. Notably, an innovative two-stage training strategy was introduced. Following the completion of the first stage, the model underwent a validation-driven fine-tuning process, essentially a "retraining" phase. This second stage aimed to further optimize model parameters and improve generalization capability. The effectiveness of the proposed method was comprehensively evaluated through a reassessment of model performance. Detailed comparative analyses of the experimental results are presented in [Figs. 4 and 5](#), and [Table 1](#), which visually and numerically demonstrate the advantages of this approach over traditional methods.

To evaluate the effectiveness of physical constraint integration and subsequent optimization in the BPINN model, two PIFNN variants were designed. BPINN-1 represents a version with only physical constraint integration but no subsequent optimization, while BPINN-2 represents the complete implementation with both physical constraint integration and subsequent optimization. To ensure a fair comparison, the total training epochs for traditional FNN, BPINN-1, and BPINN-2 were all set to 2000. PIFNN-2 adopted a two-stage training strategy: an initial phase of 1600 iterations followed by an optimization phase of 400 iterations. This strategy aims to fully utilize the guidance of physical constraints while further improving model performance through subsequent optimization. By comparing these model variants, we can analyze in depth the contributions of various components in the BPINN framework, particularly the impact of physical constraint integration and subsequent optimization on prediction accuracy. [Fig. 6](#) presents the performance evolution of the BPINN model during the two-stage training process. It shows the optimization trajectory across different dimensions and the trend of data fitting loss in both training stages. Specifically, it depicts the deviation between model predictions and actual observations on training samples. This loss value is calculated based on the loss data terms defined in Equations (13) and (15). The curve's trajectory reflects the gradual improvement process of the model in data fitting. It records the penalty loss incurred due to violations of preset physical rules during both training stages. Comparative analysis shows that both BPINN variants exhibit faster convergence in terms of physical loss and a more rapid decline in progressive real-world errors during the initial

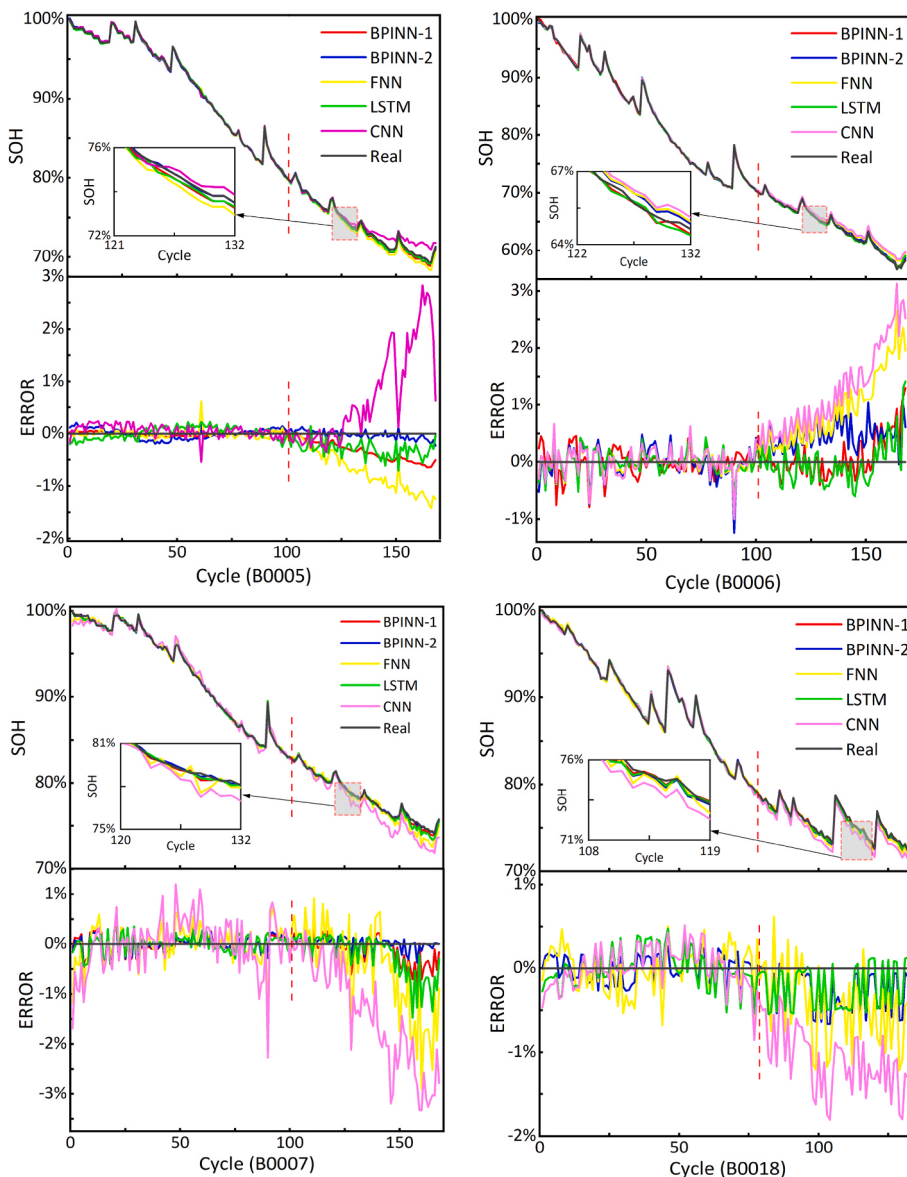


Fig. 4. SOH prediction results of different models in the NASA battery dataset.

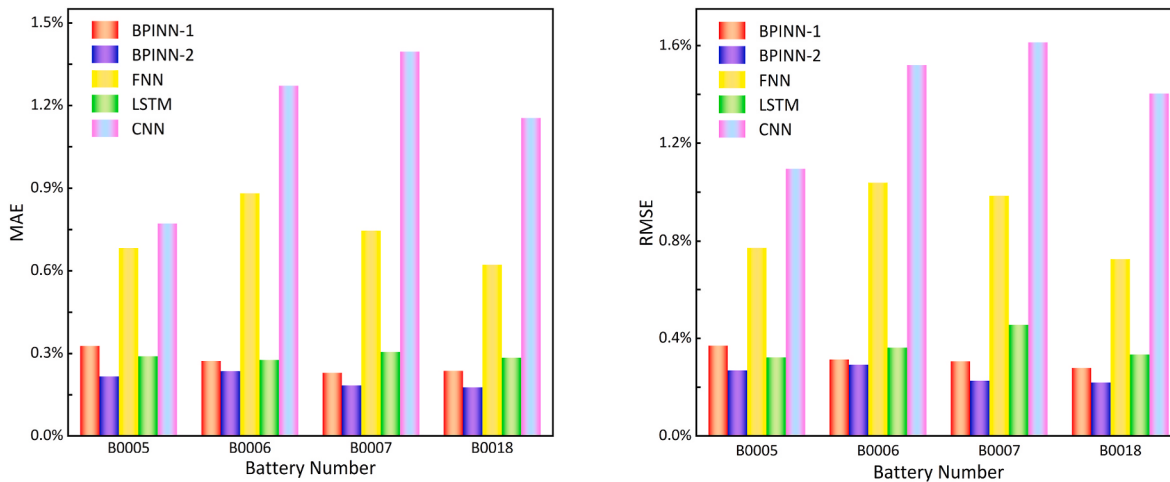


Fig. 5. Comparison of prediction errors of different models on the NASA battery dataset.

Table 1

MAE and RMSE of SOH predictions on NASA battery dataset across different models.

Battery		B0005	B0006	B0007	B0018
MAE (%)	BPINN-1	0.3274	0.2737	0.2294	0.2365
	BPINN-2	0.2164	0.2351	0.1837	0.1771
	FNN	0.6826	0.8813	0.7453	0.6216
	LSTM	0.2904	0.2773	0.3061	0.2851
	CNN	0.7714	1.2729	1.3952	1.1549
RMSE (%)	BPINN-1	0.3711	0.3146	0.3071	0.2789
	BPINN-2	0.2685	0.2937	0.2268	0.2193
	FNN	0.7734	1.0392	0.9856	0.7246
	LSTM	0.3234	0.3629	0.4556	0.3356
	CNN	1.0959	1.5205	1.6129	1.4035

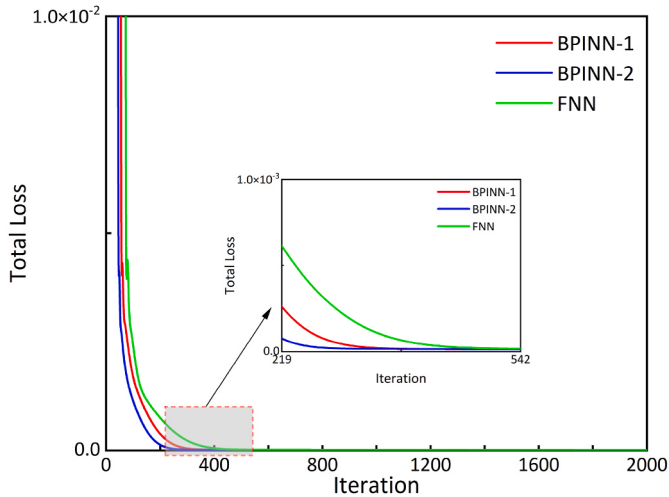


Fig. 6. Comparison of the convergence of total loss between BPINN and FNN on the NASA battery dataset.

stage. However, it's noteworthy that the traditional FNN model also achieved zero convergence in physical loss eventually. Moreover, all three models reached similar levels of true error in the later stages of training.

As shown in Fig. 4, this convergence pattern reflects to some extent the characteristics of the NASA battery dataset, particularly the relatively limited number of sampling points and regular decay curve features in each lithium-ion battery dataset, allowing FNN to achieve high accuracy on the training set as well. Initially, Equation (12) was used to express physical constraints. However, considering noise and other interfering factors in real data, the relationship between P-IC and SOH does not strictly follow a monotonic pattern. To better adapt to this reality, the expression of constraint conditions was improved. Specifically, a difference-based method was introduced, and Equation (18) was proposed as an optimized expression of physical constraints.

$$d(x^i) = \frac{\hat{g}(x^i, W, M) - \hat{g}(x^i - \Delta x, W, M)}{\Delta x} > 0 \quad (18)$$

Where Δx is the sampling interval, which needs to be manually adjusted.

Based on Fig. 4, both BPINN-1 and BPINN-2 demonstrate considerable stability in SOH prediction, particularly when the number of iterations is high, maintaining low error levels. In contrast, the CNN model exhibits a significant increase in error as the number of iterations rises, resulting in inferior predictive performance compared to the BPINN

models. The LSTM model performs relatively well, although it shows considerable error fluctuations with the B0006 battery. Overall, the integration of physical constraints in the BPINN models effectively enhances the accuracy of SOH predictions, particularly during the battery degradation process, allowing for a better capture of actual physical changes. Fig. 5 illustrates that the MAE and RMSE for BPINN-1 and BPINN-2 are significantly lower than those of other models across all batteries, especially compared to the CNN model, where the errors are reduced by approximately 70 %. This further substantiates that the introduction of physical constraints markedly improves model performance in SOH prediction. Notably, the error for BPINN-2 is slightly lower than that of BPINN-1, indicating that subsequent optimization stages effectively enhance predictive accuracy. Fig. 6 presents the loss reduction curves for the BPINN-1, BPINN-2, and FNN models over 2000 training iterations. BPINN-1 and BPINN-2 exhibit a rapid convergence rate initially, with significant loss reductions occurring within the first 400 iterations, markedly lower than that of the FNN model. This suggests that the incorporation of physical constraints plays a crucial role in accelerating model convergence. The final loss value for BPINN-2 is marginally lower than that of BPINN-1, indicating that the optimization phase further enhances the model's fitting capability. Overall, Fig. 6 validates the effectiveness of physical constraints and optimization phases, particularly in BPINN-2, where the physical constraints not only accelerate the convergence process but also improve final predictive accuracy.

The PIFNN-2 model demonstrated a significant advantage in predictive performance, surpassing both PIFNN-1 and traditional FNN models. This result strongly confirms the importance and effectiveness of the secondary optimization phase introduced in the PIFNN framework. Specifically, while maintaining similar levels of absolute error compared to other models, PIFNN-2 achieved notable improvements in overall prediction accuracy. This phenomenon highlights the critical role of the second "retraining" process in model design. This performance enhancement can be attributed to several factors:

- (1) Knowledge retention: PIFNN-2 successfully preserved the key features and pattern recognition capabilities acquired during the initial training phase.
- (2) Validation-driven optimization: By fine-tuning on the validation set, the model was better able to adapt to the feature distribution of unseen data.
- (3) Enhanced generalization: The secondary optimization process effectively reduced the model's overfitting to training data, improving its performance on new data.
- (4) Balance between physical constraints and data-driven approaches: This method allows for finer adjustments to data features while maintaining physical consistency.

In this study, we compared the performance of several mainstream deep learning models in the task of battery performance prediction. The results show that CNN showed suboptimal overall predictive performance. This can be primarily attributed to the mismatch between CNN's architectural characteristics and the temporal nature of the prediction task in this experiment. In contrast, LSTM demonstrated excellent predictive capabilities. For some battery samples, the prediction accuracy of LSTM even surpassed that of the BPINN model proposed in this study. This advantage mainly stems from LSTM's recurrent structure, which is inherently well-suited for handling time series data, giving it a unique advantage in capturing long-term dependencies. However, the LSTM model also has some limitations. The primary issue is that its predictions may violate basic physical laws, due to the model's lack of explicit

physical constraint guidance. Additionally, compared to FNN and BPINN, the LSTM's network structure is more complex, which not only reduces computational efficiency but also increases the risk of model overfitting.

3.2. Evaluation and validation with the oxford university battery dataset

To further evaluate the universality and effectiveness of the second stage in the BPINN framework, this study introduced the Oxford University Battery Dataset [48,49] as an additional validation benchmark. The Oxford research team conducted systematic cycling tests on eight Kokam brand pouch lithium-ion batteries. These batteries have a nominal capacity of 740 mAh and are labeled as Cell1 through Cell8 in the experiment. The batteries feature a composite positive electrode material of lithium nickel cobalt oxide and lithium cobalt oxide, paired with a graphite negative electrode - a configuration typical in current lithium-ion battery technology. To simulate real-world electric vehicle usage conditions, researchers designed a dynamic charge-discharge protocol. Specifically, the batteries underwent charge-discharge cycles at a 2C rate. After every 100 cycles, a standardized charging process was executed: constant current charging at 1C rate up to 4.2V, followed by a constant voltage mode until the charging current dropped to a preset cut-off value. Throughout this process, key parameters such as time (t), voltage (V), temperature (T), and current (I) were recorded in real-time. The experiment continued until the battery's state of health (SOH) decreased to 80 %, typically considered the end-of-life threshold for lithium batteries in electric vehicles. Throughout the testing process, the battery operating temperature was controlled to fluctuate between 39 °C and 41 °C, simulating thermal management conditions in practical applications. Figs. 7 and 8(a), and Table 2 present the performance evaluation results of the BPINN model on the Oxford University battery

dataset. Fig. 8(b) represents the same content as Fig. 6. To thoroughly investigate the impact of the second-stage training in the BPINN framework, two variant models were introduced: BPINN-1 and BPINN-2. Both models maintain consistency in total iterations at 2000, but differ significantly in training strategy. BPINN-1: Represents a model version without second-stage optimization, employing a uniform training strategy throughout. BPINN-2: Adopts a two-stage training method. Specifically, the first 1600 iterations constitute the initial training phase, while the subsequent 400 iterations are considered the optimization phase.

Firstly, examining Fig. 8(b), the physical loss value in the Oxford University battery dataset is consistently greater than zero. Additionally, compared to FNN, PIFNN demonstrates superior accuracy during the training phase. This can be attributed to the richer sampling data in the NASA database. Further analysis of Fig. 8(b) reveals that throughout the training process, the rate of decrease in the physical loss value for PIFNN surpasses that of FNN after introducing physical constraints. The actual error of PIFNN also shows a faster decreasing trend. Figs. 7 and 8(a) further corroborate that PIFNN-1 is more accurate than FNN, highlighting the effectiveness of the second phase of PIFNN in handling complex battery databases. Similarly, comparing PIFNN-1 and PIFNN-2, it is evident that they exhibit almost identical accuracy and rates of physical loss reduction. This similarity is due to the limited restrictive capability of the introduced physical constraints. When the model has already achieved high accuracy in training and prediction, and the loss value for violating physical constraints is low, there is limited room for further improvement. This is particularly evident in PIFNN-2, which shows similar suboptimal performance observed in the NASA battery dataset. The introduced physical constraints have limited binding power, and the weight assigned to the physical loss value is small, underscoring the need for fine-tuning the model.

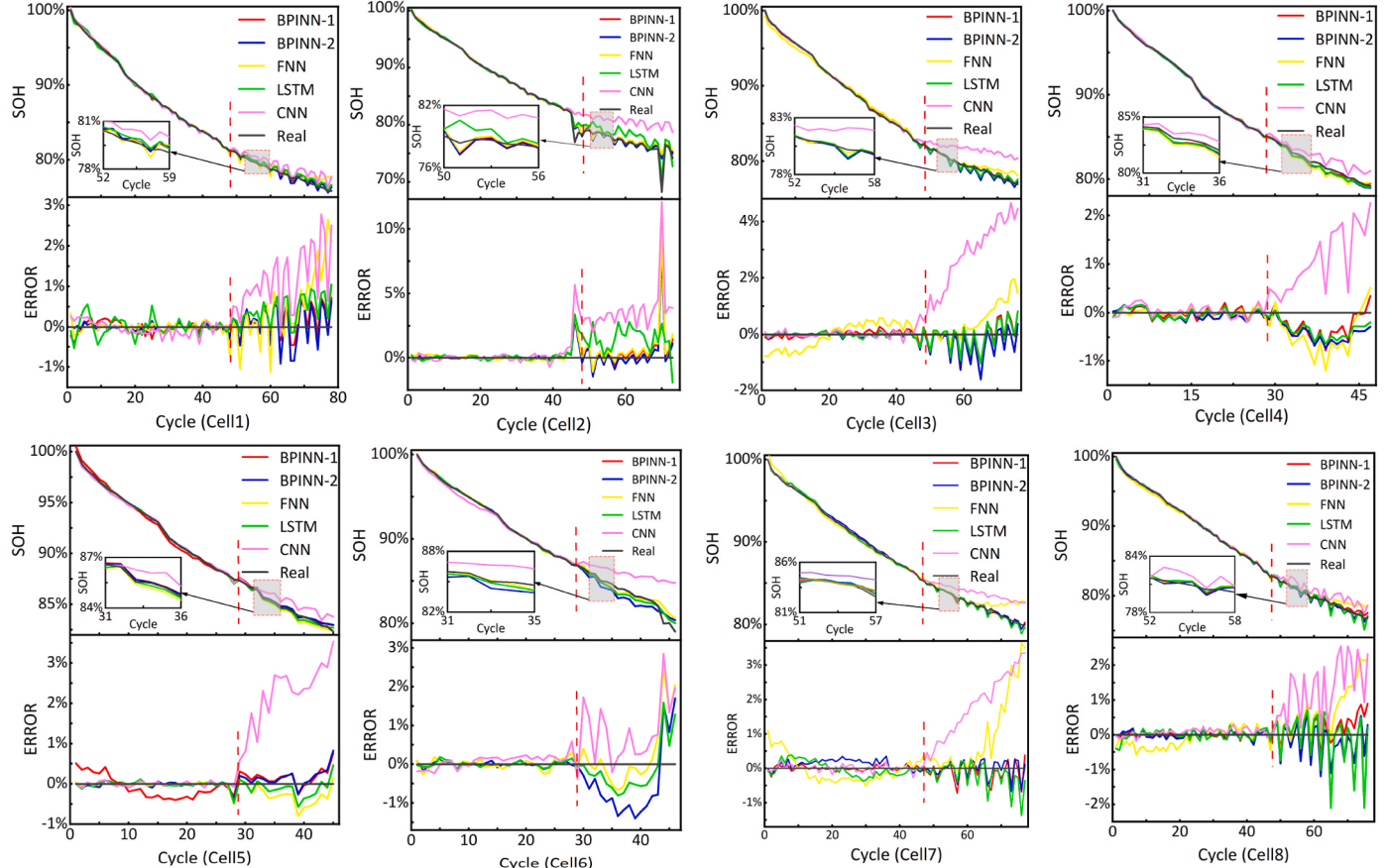


Fig. 7. Comparison of prediction performance of different models on the Oxford University battery dataset.

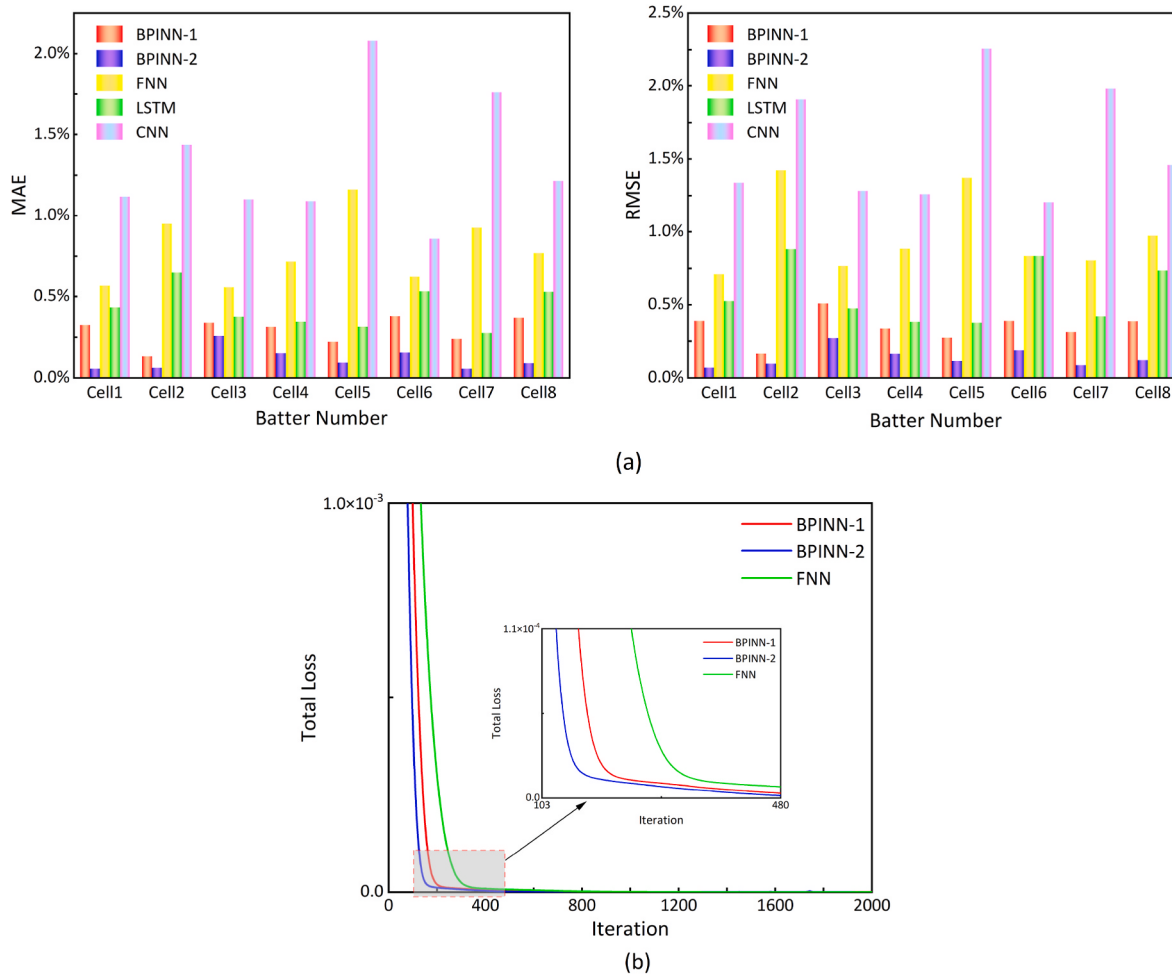


Fig. 8. Comparison of Prediction Errors and Convergence of Total Loss on the Oxford University Battery Dataset: (a) Comparison of prediction errors of different models on the Oxford University battery dataset. (b) Comparison of the convergence of total loss between BPINN and FNN on the Oxford University battery dataset.

Table 2

MAE and RMSE of SOH predictions on Oxford University battery dataset across different models.

Battery	Cell 1	Cell 2	Cell 3	Cell 4	Cell 5	Cell 6	Cell 7	Cell 8	
MAE (%)	BPINN-1	0.3256	0.1336	0.3388	0.3135	0.2224	0.3791	0.2396	0.3692
	BPINN-2	0.0576	0.0632	0.2570	0.1522	0.0942	0.1566	0.0570	0.0911
	FNN	0.5684	0.9496	0.5578	0.7156	1.1614	0.6248	0.9252	0.7659
	LSTM	0.4327	0.6496	0.3762	0.3452	0.3149	0.5322	0.2756	0.5295
	CNN	1.1178	1.4369	1.1010	1.0900	2.0811	0.8572	1.7607	1.2149
RMSE (%)	BPINN-1	0.3888	0.1658	0.5080	0.3370	0.2748	0.3888	0.3134	0.3872
	BPINN-2	0.0717	0.0978	0.2705	0.1648	0.1159	0.1888	0.0880	0.1222
	FNN	0.7112	1.4221	0.7663	0.8847	1.3711	0.8341	0.8041	0.9732
	LSTM	0.5244	0.8821	0.4742	0.3821	0.3771	0.8341	0.4200	0.7352
	CNN	1.3369	1.9083	1.2823	1.2592	2.2564	1.2026	1.9809	1.4584

Compared to traditional neural networks like LSTM and CNN, PIFNN demonstrates similar predictive capabilities on the Oxford University battery dataset. However, one major advantage of PIFNN is its stronger interpretability, making it easier to understand and apply.

4. Conclusion

This paper proposes a novel physically constrained SOH estimation method. This method first extracts six features from the IC curve during the battery discharge process and uses the monotonic relationship between the peak features obtained from the IC curve and the SOH as constraint conditions to enhance the training process of the FNN. During

the prediction phase, we further optimize the model by performing a second “training” to reduce the occurrence of physical constraint violations in the purely data-driven model on the test set. Experimental results show that this method effectively improves the interpretability and accuracy of the FNN. Comparative experiments conducted on the NASA and Oxford University battery datasets demonstrate that when the FNN’s predictions on the training set severely violate physical constraints, BPINN significantly enhances prediction accuracy by incorporating physical information guidance. Moreover, during the testing phase, BPINN with secondary “training” effectively reduces the occurrence of physical constraint violations, thereby further improving prediction accuracy.

CRediT authorship contribution statement

Guoqing Sun: Writing – original draft, Software, Methodology, Conceptualization. **Yafei Liu:** Visualization, Data curation. **Xuewen Liu:** Writing – review & editing, Supervision, Conceptualization.

Funding

No funding was received for conducting this study.

Declaration of competing interest

The authors declare no conflicts of interest.

Data availability

Data will be made available on request.

References

- [1] S. Kohtz, Y. Xu, Z. Zheng, P. Wang, Physics-informed machine learning model for battery state of health prognostics using partial charging segments, *Mech. Syst. Signal Process.* 172 (2022) 109002, <https://doi.org/10.1016/j.ymssp.2022.109002>.
- [2] X. Tang, X. Lai, C. Zou, Y. Zhou, J. Zhu, Y. Zheng, F. Gao, Detecting abnormality of battery lifetime from first-cycle data using few-shot learning, *Adv. Sci.* 11 (6) (2024) 2305315, <https://doi.org/10.1002/advs.202305315>.
- [3] S. Wang, S. Jin, D. Bai, Y. Fan, H. Shi, C. Fernandez, A critical review of improved deep learning methods for the remaining useful life prediction of lithium-ion batteries, *Energy Rep.* 7 (2021) 5562–5574, <https://doi.org/10.1016/j.egyr.2021.08.182>.
- [4] K.W.E. Cheng, B.P. Divakar, H. Wu, K. Ding, H.F. Ho, Battery-management system (BMS) and SOC development for electrical vehicles, *IEEE Trans. Veh. Technol.* 60 (1) (2010) 76–88, <https://doi.org/10.1109/TVT.2010.2089647>.
- [5] J. Wu, C. Zhang, Z. Chen, An online method for lithium-ion battery remaining useful life estimation using importance sampling and neural networks, *Appl. Energy* 173 (2016) 134–140, <https://doi.org/10.1016/j.apenergy.2016.04.057>.
- [6] H. Dai, G. Zhao, M. Lin, J. Wu, G. Zheng, A novel estimation method for the state of health of lithium-ion battery using prior knowledge-based neural network and Markov chain, *IEEE Trans. Ind. Electron.* 66 (10) (2018) 7706–7716, <https://doi.org/10.1109/TIE.2018.2880703>.
- [7] Z. Xu, Y. Guo, J.H. Saleh, A physics-informed dynamic deep autoencoder for accurate state-of-health prediction of lithium-ion battery, *Neural Comput. Appl.* 34 (18) (2022) 15997–16017, <https://doi.org/10.1007/s00521-022-07291-5>.
- [8] H. Meng, M. Geng, J. Xing, E. Zio, A hybrid method for prognostics of lithium-ion batteries capacity considering regeneration phenomena, *Energy* 261 (2022) 125278, <https://doi.org/10.1016/j.energy.2022.125278>.
- [9] Y. Wang, C. Zhang, Z. Chen, On-line battery state-of-charge estimation based on an integrated estimator, *Appl. Energy* 185 (2017) 2026–2032, <https://doi.org/10.1016/j.apenergy.2015.09.015>.
- [10] X. Lai, M. Yuan, X. Tang, Y. Zheng, J. Zhu, Y. Sun, F. Gao, State-of-power estimation for lithium-ion batteries based on a frequency-dependent integer-order model, *J. Power Sources* 594 (2024) 234000, <https://doi.org/10.1016/j.jpowsour.2023.234000>.
- [11] S. Yang, C. Zhang, J. Jiang, W. Zhang, L. Zhang, Y. Wang, Review on state-of-health of lithium-ion batteries: characterizations, estimations and applications, *J. Clean. Prod.* 314 (2021) 128015, <https://doi.org/10.1016/j.jclepro.2021.128015>.
- [12] J. Liang, H. Liu, N.C. Xiao, A hybrid approach based on deep neural network and double exponential model for remaining useful life prediction, *Expert Syst. Appl.* 249 (2024) 123563, <https://doi.org/10.1016/j.eswa.2024.123563>.
- [13] E. Prada, D. Di Domenico, Y. Creff, J. Bernard, V. Sauvant-Moynot, F. Huet, Simplified electrochemical and thermal model of LiFePO₄-graphite Li-ion batteries for fast charge applications, *J. Electrochem. Soc.* 159 (9) (2012) A1508, <https://doi.org/10.1149/2.064209jes>.
- [14] S. Chen, Q. Zhang, F. Wang, D. Wang, Z. He, An electrochemical-thermal-aging effects coupled model for lithium-ion batteries performance simulation and state of health estimation, *Appl. Therm. Eng.* 239 (2024) 122128, <https://doi.org/10.1016/j.applthermaleng.2023.122128>.
- [15] G.H. Kim, K. Smith, K.J. Lee, S. Santhanagopalan, A. Pesaran, Multi-domain modeling of lithium-ion batteries encompassing multi-physics in varied length scales, *J. Electrochem. Soc.* 158 (8) (2011) A955, <https://doi.org/10.1149/1.3597614>.
- [16] Z. Xu, J. Wang, P.D. Lund, Y. Zhang, Co-estimating the state of charge and health of lithium batteries through combining a minimalist electrochemical model and an equivalent circuit model, *Energy* 240 (2022) 122815, <https://doi.org/10.1016/j.energy.2021.122815>.
- [17] Y. Li, K. Liu, A.M. Foley, A. Zülke, M. Berecibar, E. Nanini-Maury, H.E. Hostler, Data-driven health estimation and lifetime prediction of lithium-ion batteries: a review, *Renew. Sustain. Energy Rev.* 113 (2019) 109254, <https://doi.org/10.1016/j.rser.2019.109254>.
- [18] G. Sun, Y. Liu, X. Liu, A neural network approach for health state estimation of lithium-ion batteries incorporating physics knowledge, *Electron. Mater. Lett.* (2024) 1–15, <https://doi.org/10.1007/s13391-024-00518-8>.
- [19] C. Zhang, L. Luo, Z. Yang, S. Zhao, Y. He, X. Wang, H. Wang, *GEIT* 2 (5) (2023) 100108, <https://doi.org/10.1016/j.geits.2023.100108>.
- [20] L. Vichard, A. Ravey, P. Venet, F. Harel, S. Pelissier, D. Hissel, A method to estimate battery SOH indicators based on vehicle operating data only, *Energy* 225 (2021) 120235, <https://doi.org/10.1016/j.energy.2021.120235>.
- [21] S. Peng, Y. Sun, D. Liu, Q. Yu, J. Kan, M. Pecht, State of health estimation of lithium-ion batteries based on multi-health features extraction and improved long short-term memory neural network, *Energy* 282 (2023) 128956, <https://doi.org/10.1016/j.energy.2023.128956>.
- [22] R. Pan, T. Liu, W. Huang, Y. Wang, D. Yang, J. Chen, State of health estimation for lithium-ion batteries based on two-stage features extraction and gradient boosting decision tree, *Energy* 285 (2023) 129460, <https://doi.org/10.1016/j.energy.2023.129460>.
- [23] G. Ma, S. Xu, T. Yang, Z. Du, L. Zhu, H. Ding, Y. Yuan, A transfer learning-based method for personalized state of health estimation of lithium-ion batteries, *IEEE Transact. Neural Networks Learn. Syst.* 35 (1) (2022) 759–769, <https://doi.org/10.1109/TNNLS.2022.3176925>.
- [24] X.Y. Yao, G. Chen, M. Pecht, B. Chen, A novel graph-based framework for state of health prediction of lithium-ion battery, *J. Energy Storage* 58 (2023) 106437, <https://doi.org/10.1016/j.est.2022.106437>.
- [25] H. Dai, G. Zhao, M. Lin, J. Wu, G. Zheng, A novel estimation method for the state of health of lithium-ion battery using prior knowledge-based neural network and Markov chain, *IEEE Trans. Ind. Electron.* 66 (10) (2018) 7706–7716, <https://doi.org/10.1109/TIE.2018.2880703>.
- [26] H. Jiang, X. Lv, K. Wang, Application of triboelectric nanogenerator in self-powered motion detection devices: a review, *Apl. Mater.* 12 (2024), <https://doi.org/10.1063/5.0219633>.
- [27] Y. Shang, S. Wang, N. Tang, Y. Fu, K. Wang, Research progress in fault detection of battery systems: a review, *J. Energy Storage* 98 (2024) 113079, <https://doi.org/10.1016/j.est.2024.113079>.
- [28] S. Cui, S. Lyu, Y. Ma, K. Wang, Improved informer PV power short-term prediction model based on weather typing and AHA-VMD-MPE, *Energy* 307 (2024) 132766, <https://doi.org/10.1016/j.energy.2024.132766>.
- [29] G. Qi, N. Ma, K. Wang, Predicting the remaining useful life of supercapacitors under different operating conditions, *Energies* 17 (2024) 2585, <https://doi.org/10.3390/en17112585>.
- [30] K.A. Severson, P.M. Attia, N. Jin, N. Perkins, B. Jiang, Z. Yang, R.D. Braatz, Data-driven prediction of battery cycle life before capacity degradation, *Nat. Energy* 4 (5) (2019) 383–391, <https://doi.org/10.1038/s41560-019-0356-8>.
- [31] S. Kohtz, Y. Xu, Z. Zheng, P. Wang, Physics-informed machine learning model for battery state of health prognostics using partial charging segments, *Mech. Syst. Signal Process.* 172 (2022) 109002, <https://doi.org/10.1016/j.ymssp.2022.109002>.
- [32] T. Hofmann, J. Hamar, M. Rogge, C. Zoerr, S. Erhard, J.P. Schmidt, Physics-informed neural networks for state of health estimation in lithium-ion batteries, *J. Electrochem. Soc.* 170 (9) (2023) 090524, <https://doi.org/10.1149/1945-7111/ac0ef>.
- [33] F. Wang, Z. Zhai, Z. Zhao, Y. Di, X. Chen, Physics-informed neural network for lithium-ion battery degradation stable modeling and prognosis, *Nat. Commun.* 15 (2024) 4332, <https://doi.org/10.1038/s41467-024-48779-z>.
- [34] S.B. Vilsen, D.I. Stroe, Transfer learning for adapting battery state-of-health estimation from laboratory to field operation, *IEEE Access* 10 (2022) 26514–26528, <https://doi.org/10.1109/ACCESS.2022.3156657>.
- [35] J. Ye, Q. Xie, M. Lin, J. Wu, A method for estimating the state of health of lithium-ion batteries based on physics-informed neural network, *Energy* 294 (2024) 130828, <https://doi.org/10.1016/j.energy.2024.130828>.
- [36] X. Hu, S. Li, H. Peng, A comparative study of equivalent circuit models for Li-ion batteries, *J. Power Sources* 198 (2012) 359–367, <https://doi.org/10.1016/j.jpowsour.2011.10.013>.
- [37] M. Ecker, J.B. Gerschler, J. Vogel, S. Käbitz, F. Hust, P. Dechant, D.U. Sauer, Development of a lifetime prediction model for lithium-ion batteries based on extended accelerated aging test data, *J. Power Sources* 215 (2012) 248–257, <https://doi.org/10.1016/j.jpowsour.2012.05.012>.
- [38] P. Keil, A. Jossen, Charging protocols for lithium-ion batteries and their impact on cycle life—an experimental study with different 18650 high-power cells, *J. Energy Storage* 6 (2016) 125–141, <https://doi.org/10.1016/j.est.2016.02.005>.
- [39] M. Berecibar, I. Gandiaga, I. Villarreal, N. Omar, J. Van Mierlo, P. Van den Bossche, Critical review of state of health estimation methods of Li-ion batteries for real applications, *Renew. Sustain. Energy Rev.* 56 (2016) 572–587, <https://doi.org/10.1016/j.rser.2015.11.042>.
- [40] B. Saha, K. Goebel, Battery data set. NASA Ames Prognostics Data Repository, NASA Ames Research Center, Moffett Field, CA, 2007. <http://ti.arc.nasa.gov/project/%2620prognostic-data-repository>.
- [41] L. Zheng, J. Zhu, D.D.C. Lu, G. Wang, T. He, Incremental capacity analysis and differential voltage analysis based state of charge and capacity estimation for lithium-ion batteries, *Energy* 150 (2018) 759–769, <https://doi.org/10.1016/j.energy.2018.03.023>.
- [42] N. Omar, M.A. Monem, Y. Firouz, J. Salminen, J. Smekens, O. Hegazy, J. Van Mierlo, Lithium iron phosphate based battery—Assessment of the aging parameters and development of cycle life model, *Appl. Energy* 113 (2014) 1575–1585, <https://doi.org/10.1016/j.apenergy.2013.09.003>.

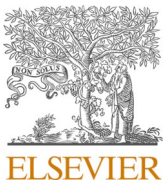
- [43] C.R. Birkl, M.R. Roberts, E. McTurk, P.G. Bruce, D.A. Howey, Degradation diagnostics for lithium ion cells, *J. Power Sources* 341 (2017) 373–386, <https://doi.org/10.1016/j.jpowsour.2016.12.011>.
- [44] D. Anseán, V.M. García, M. González, C. Blanco-Viejo, J.C. Viera, Y.F. Pulido, L. Sánchez, Lithium-ion battery degradation indicators via incremental capacity analysis, *IEEE Trans. Ind. Appl.* 55 (3) (2019) 2992–3002, <https://doi.org/10.1109/TIA.2019.2891213>.
- [45] J. Vetter, P. Novák, M.R. Wagner, C. Veit, K.C. Möller, J.O. Besenhard, A. Hammouche, Ageing mechanisms in lithium-ion batteries, *J. Power Sources* 147 (1–2) (2005) 269–281, <https://doi.org/10.1016/j.jpowsour.2005.01.006>.
- [46] C. Pastor-Fernández, W.D. Widanage, J. Marco, M.A. Gama-Valdez, G. H. Chouchelamane, Identification and quantification of ageing mechanisms in Lithium-ion batteries using the EIS technique, in: 2016 IEEE Transportation Electrification Conference and Expo (ITEC), 2016, June, pp. 1–6, <https://doi.org/10.1109/ITEC.2016.7520198>. IEEE.
- [47] Y. Liu, G. Sun, X. Liu, Remaining useful life prediction of lithium-ion batteries based on peak interval features and deep learning, *J. Energy Storage* 73 (2023) 109308, <https://doi.org/10.1016/j.est.2023.109308>.
- [48] C. Birkl, Diagnosis and Prognosis of Degradation in Lithium-Ion Batteries (Doctoral Dissertation, University of Oxford), 2017, <https://doi.org/10.5287/bodleian:KO2kdmYGg>.
- [49] C. Birkl, Oxford Battery Degradation Dataset 1, University of Oxford, 2017, <https://doi.org/10.5287/bodleian:KO2kdmYGg>.

Update

Journal of Power Sources

Volume 630, Issue , 28 February 2025, Page

DOI: <https://doi.org/10.1016/j.jpowsour.2024.236161>



Corrigendum to “A method for estimating lithium-ion battery state of health based on physics-informed machine learning” [J. Power Sour. 627 (2025) 235767]

Guoqing Sun, Yafei Liu, Xuewen Liu ^{*}

School of Mechanical and Automotive Engineering, Shanghai University of Engineering Science, Shanghai, 201600, China

The authors regret the following errors in the original article titled "A Method for Estimating Lithium-Ion Battery State of Health Based on Physics-Informed Machine Learning" (Manuscript ID: POWER-D-24-03759R2):

● Incorrect Term Usage: In the original manuscript, the term "PIFNN" was mistakenly used instead of the correct term "BPINN" (Battery Physics-Informed Neural Network). This error occurred due to an inadvertent reference to [35] during the writing process, where the incorrect term was carried over. The authors kindly request the editor to replace all instances of "PIFNN" with "BPINN" throughout the manuscript (a total of 17 occurrences).

- **Typographical Error:** There is a typographical error in section 3.2, where the term "second-s5tage" is used. The correct term is "second-stage," and the authors request this correction to be made in the manuscript.
- **Incorrect Dataset Reference:** In section 3.2, the sentence "This can be attributed to the richer sampling data in the NASA database" mistakenly references the "NASA database." The correct dataset should be the "Oxford University dataset." The authors request this correction to be made in the manuscript.

The authors would like to apologise for any inconvenience caused.



DOI of original article: <https://doi.org/10.1016/j.jpowsour.2024.235767>.

* Corresponding author.

E-mail address: xuewen2018@126.com (X. Liu).